Little red dots at an inflection point: ubiquitous V-shaped turnover consistently occurs at the Balmer limit

Setton, D.J.; Greene, J.E.; de Graaff, A.; Ma, Y.; Leja, J.; Matthee, J.; ... ; Williams, C.C.

The Astrophysical Journal, 995:118 (13pp), 2025 December 10 https://doi.org/10.3847/1538-4357/ae1500

Little Red Dots at an Inflection Point: Ubiquitous V-shaped Turnover Consistently Occurs at the Balmer Limit

David J. Setton[1,20], Jenny E. Greene[1], Anna de Graaff[2], Yilun Ma (马逸伦)[1], Joel Leja[3,4,5], Jorryt Matthee[6], Rachel Bezanson[7], Leindert A. Boogaard[8], Nikko J. Cleri[3,4,5], Harley Katz[9,10], Ivo Labbe[11], Michael V. Maseda[12], Ian McConachie[12], Tim B. Miller[13], Sedona H. Price[7], Katherine A. Suess[14], Pieter van Dokkum[15], Bingjie Wang (王冰洁)[3,4,5], Andrea Weibel[16], Katherine E. Whitaker[17,18], and Christina C. Williams[19]
[1] Department of Astrophysical Sciences, Princeton University, 4 Ivy Lane, Princeton, NJ 08544, USA; davidsetton@princeton.edu
[2] Max-Planck-Institut für Astronomie, Königstuhl 17, D-69117, Heidelberg, Germany
[3] Department of Astronomy & Astrophysics, The Pennsylvania State University, University Park, PA 16802, USA
[4] Institute for Computational & Data Sciences, The Pennsylvania State University, University Park, PA 16802, USA
[5] Institute for Gravitation and the Cosmos, The Pennsylvania State University, University Park, PA 16802, USA
[6] Institute of Science and Technology Austria (ISTA), Am Campus 1, Klosterneuburg, Austria
[7] Department of Physics and Astronomy and PITT PACC, University of Pittsburgh, Pittsburgh, PA 15260, USA
[8] Leiden Observatory, Leiden University, PO Box 9513, NL-2300 RA Leiden, The Netherlands
[9] Department of Astronomy & Astrophysics, University of Chicago, 5640 S Ellis Avenue, Chicago, IL 60637, USA
[10] Kavli Institute for Cosmological Physics, University of Chicago, Chicago, IL 60637, USA
[11] Centre for Astrophysics and Supercomputing, Swinburne University of Technology, Melbourne, VIC 3122, Australia
[12] Department of Astronomy, University of Wisconsin-Madison, 475 N. Charter St., Madison, WI 53706, USA
[13] Center for Interdisciplinary Exploration and Research in Astrophysics (CIERA), Northwestern University, 1800 Sherman Ave, Evanston, IL 60201, USA
[14] Department for Astrophysical & Planetary Science, University of Colorado, Boulder, CO 80309, USA
[15] Astronomy Department, Yale University, 219 Prospect St, New Haven, CT 06511, USA
[16] Department of Astronomy, University of Geneva, Chemin Pegasi 51, 1290 Versoix, Switzerland
[17] Department of Astronomy, University of Massachusetts, Amherst, MA 01003, USA
[18] Cosmic Dawn Center (DAWN), Denmark
[19] NSF National Optical-Infrared Astronomy Research Laboratory, 950 North Cherry Avenue, Tucson, AZ 85719, USA
Received 2024 November 6; revised 2025 October 16; accepted 2025 October 17; published 2025 December 9

Abstract

Among the most puzzling early discoveries of JWST are "little red dots" (LRDs), compact red sources that host broad Balmer emission lines, and in many cases exhibit a "V-shaped" change in slope in the rest-optical. The physical properties of LRDs currently have order-of-magnitude uncertainties, because models to explain the continuum of these sources differ immensely. Here, we leverage the complete selection of red sources in the RUBIES program, supplemented with public PRISM spectra, to study the origin of this V shape. By fitting a broken power law with a flexible inflection point, we find that a large fraction of red Hα emitters at $2 < z < 6$ exhibit a strong change in slope, and that all strong inflections appear associated with the Balmer limit (0.3645 μm). Using a simple model of a reddened active galactic nucleus (AGN) with an unobscured scattered-light component, we demonstrate that the observed V shape in LRDs is unlikely to occur at any specific wavelength if the entire continuum is dominated by light from a power-law AGN continuum. In contrast, models with an intrinsic feature at the Balmer limit, such as those that are dominated by an evolved stellar population, can produce the observed spectral shapes, provided that a reddened component picks up sufficiently redward of the break. While no model can comfortably explain the full LRD spectral energy distribution, the common inflection location suggests that a single component consistently dominates the rest-frame UV optical in LRDs, and that this component is associated with $T \sim 10^4$ K hydrogen.

Unified Astronomy Thesaurus concepts: Active galactic nuclei (16); High-redshift galaxies (734); Galaxy evolution (594); Near infrared astronomy (1093)

Materials only available in the online version of record: machine-readable table

1. Introduction

One of the most intriguing discoveries in the first few years of JWST observations has been large numbers of compact red sources (e.g., I. Labbé et al. 2023, 2025; G. Barro et al. 2024). Follow-up spectroscopy has revealed that these sources often contain broad Balmer emission lines with FWHM > 2000 km s^{-1} (M. Killi et al. 2024; V. Kokorev et al. 2023; R. L. Larson et al. 2023; J. E. Greene et al. 2024; H. Übler et al. 2024; B. Wang et al. 2024b, 2025). At the same time, spectroscopically identified broad-line objects are commonly red and compact (Y. Harikane et al. 2023; D. D. Kocevski et al. 2025; X. Lin et al. 2024), leading J. Matthee et al. (2024) to dub this new class of sources "little red dots" (LRDs). Not only do the sources share a compact morphology (being effectively unresolved in the rest-frame optical, implying $r_e \lesssim 100$ pc), many sources have a characteristic "V shape," wherein the red rest-frame optical slope transitions to a blue rest-frame UV slope. These objects have become the subject of intense study because they are so common, with characteristic number densities $\sim 5 \times 10^{-5}$ Mpc^{-3} at $z = 4$–8

[20] Brinson Prize Fellow.

(e.g., V. Kokorev et al. 2024); they account for a few percent of $>L_*$ galaxies, and at least 20% of active galactic nuclei (AGN) with broad lines (Y. Harikane et al. 2023).

Early photometric papers favored the hypothesis that these objects are AGN based on their compact morphology (e.g., M. Onoue et al. 2023; L. J. Furtak et al. 2024; I. Labbe et al. 2025), later supported by early spectroscopic papers that used the presence of broad emission lines as support for an AGN hypothesis (L. J. Furtak et al. 2024; J. Matthee et al. 2024; H. Übler et al. 2024). However, there has always been some ambiguity about whether the red continuum is dominated by an evolved stellar population (I. Labbé et al. 2023; J. F. W. Baggen et al. 2024; G. Barro et al. 2024; P. G. Pérez-González et al. 2024; C. C. Williams et al. 2024). Despite spectroscopic follow-up of some sources showing clear evidence for a Balmer break (which could imply that stellar continuum dominates in the rest-optical), it is not clear how such a break and broad lines can coexist (B. Wang et al. 2024b; Y. Ma et al. 2025). The lack of strong X-ray detections (H. B. Akins et al. 2025; T. T. Ananna et al. 2024; L. J. Furtak et al. 2024; R. Maiolino et al. 2025; M. Yue et al. 2024) and apparent lack of variability (M. Kokubo & Y. Harikane 2024), combined with the lack of hot dust emission out to rest-frame 3–4 μm (H. B. Akins et al. 2025; B. Wang et al. 2025; C. C. Williams et al. 2024), also seems to point to a stellar origin for the rest-optical LRD continuum. However, it is challenging for the stellar-only model to account for the presence of the highly luminous broad Balmer emission, especially given that the nondetection of these sources in the far-IR (FIR) seems to disfavor buried star formation (e.g., H. B. Akins et al. 2025; C. C. Williams et al. 2024; I. Labbe et al. 2025). Thus, at this moment, there is no consensus on the nature of the LRDs.

Most of the works referenced above have modeled the photometric colors of LRDs. Spectroscopy may provide additional important insight into the continuum shape of these systems, particularly with regard to the V-shaped change in slope that LRDs are selected to have. The Red Unknowns: Bright Infrared Extragalactic Survey (RUBIES) program with JWST/NIRSpec (JWST-GO #4233, PIs: A. de Graaff and G. Brammer; see A. de Graaff et al. 2025a) has systematically targeted the reddest distant objects in the Ultra Deep Survey (UDS) and extended groth strip (EGS) fields with continuum emission in NIRSpec/PRISM spectroscopy at 1–5 μm. In conjunction with the many other programs that observed LRDs to similar or greater depths (with public spectra now hosted at the Dawn JWST Archive, DJA[21]; A. de Graaff et al. 2025a), it is now possible to systematically study the continuum shape of LRDs in the rest-UV and rest-optical.

In this work, we utilize PRISM spectroscopy to study the continuum shape of LRDs in detail, with the primary goal of determining where the pivot of the V shape occurs. In Section 2, we describe the spectroscopic and imaging sample that we use for this work. In Section 3, we describe our methods for identifying extremely red Hα-emitting sources and our continuum fitting method to determine the inflection location in the sources. In Section 4, we discuss a range of physical models and their ability to replicate the observed LRD shape we identify. Finally, in Section 5, we discuss how our findings about the rest-optical spectral shape relate to studies of the full LRD spectral energy distribution (SED). Throughout this work, we adopt the best-fit cosmological parameters from the WMAP 9 yr results (G. Hinshaw et al. 2013): $H_0 = 69.32\,\mathrm{km\,s^{-1}\,Mpc^{-1}}$, $\Omega_m = 0.2865$, and $\Omega_\Lambda = 0.7135$, utilize a Chabrier initial mass function (G. Chabrier 2003), and quote AB magnitudes.

2. Data

2.1. JWST/NIRSpec Spectroscopy

We obtain low-resolution ($R \sim 100$) JWST/NIRSpec PRISM spectra from version 3 of the DJA. These data were reduced using the latest version of `msaexp` (G. Brammer 2023a), described in detail in A. de Graaff et al. (2025a). There are two different background subtraction strategies for version 3 of the DJA; for RUBIES, we use spectra reduced with local background subtraction from nodded exposures, whereas for other programs, we use the default reductions in the DJA that were informed by the primary science goals of the programs. We note that we do not apply any additional slit-loss corrections to the spectra beyond those implemented in `msaexp`.

Our primary sample comes from RUBIES. The highest-priority targets in RUBIES are bright ($m_{\mathrm{F444W}} < 27$) and red ($m_{\mathrm{F150W}} - m_{\mathrm{F444W}} > 2$), which naturally yields a large sample of LRD-like colors. The full observing strategy is described in detail in A. de Graaff et al. (2025a).

We supplement the RUBIES sample with all public PRISM spectra available in the DJA at the time of completion of RUBIES. For both data sets, we select all spectra with a robust spectroscopic redshift $z > 2$ (`grade=3` from visual inspection in the DJA), which ensures adequate rest-UV coverage to study the continuum of these systems, and median signal-to-noise-per-pixel > 1. We additionally impose a magnitude limit of 26.5 in F444W imaging (see the following section). This yields 713 sources from RUBIES and 2463 sources from a variety of other programs. Our primary analysis includes spectra from the following programs: JADES (JWST-GTO #1180, PI: D. Eisenstein; JWST-GTO #1181, PI: D. Eistenstein; JWST-GTO #1210, PI: N. Luetzgendorf; D. J. Eisenstein et al. 2023; A. J. Bunker et al. 2024), WIDE (JWST-GTO #1211, PI: K. Isaak; M. V. Maseda et al. 2024), JWST-GO #1433 (PI: D. Coe; A. K. Meena et al. 2023), JWST-GO #2198 (PI: L. Barrufet; L. Barrufet et al. 2025), UNCOVER (JWST-GO #2561, PIs: Labbe and Bezanson; R. Bezanson et al. 2024; S. H. Price et al. 2025), JWST-GO #2565 (PI: K. Glazebrook; K. Glazebrook et al. 2024; T. Nanayakkara et al. 2024), JWST-DDT #2750 (PI: Arrabal Haro; P. Arrabal Haro et al. 2023), JWST-DDT #6858 (PI: D. Coulter), CAPERS (JWST-GO #6368, PI: M. Dickinson).

2.2. F444W Imaging

We obtain NIRCam/F444W cutouts for all galaxies with public JWST/NIRCam imaging by querying the public NIRCam mosaics hosted on the DJA, reduced with `grizli` (G. Brammer 2023b),[22] as described in detail in F. Valentino et al. (2023). We measure the F444W fluxes in a $0\farcs3$ aperture centered at the R.A. and decl. of the sources as specified in the DJA. We will also utilize these images to quantify whether these sources are extended.

[21] https://s3.amazonaws.com/msaexp-nirspec/extractions/nirspec_graded_v3.html

[22] https://grizli-cutout.herokuapp.com/

3. Analysis

In this work, we seek to broadly study the continuum shape of LRDs. A number of photometric LRD selection methods have been proposed in the literature, ranging from those using photometric colors (H. B. Akins et al. 2025; J. E. Greene et al. 2024; V. Kokorev et al. 2024; I. Labbe et al. 2025) to slopes measured from the photometry (D. D. Kocevski et al. 2025). Here, we step back from any cuts that enforce the presence of a V shape or compactness and instead employ a simple set of cuts to select a pure red sample that is emitting strongly in Hα. From this sample, we then apply a number of further cuts (e.g., a determination of whether or not the source has a V shape or is compact, meeting the definition of a LRD) to determine how common LRDs are among this extremely red sample and what features in the continuum shape these LRDs share in common. We note that one angle that we do not explore in depth is the width of Hα—this is predominantly due to the resolution limit of the PRISM spectra, which typically have $R \sim 100$ at the wavelength of Hα in this sample. However, in complementary work taking advantage of the G395M RUBIES data, R. E. Hviding et al. (2025) demonstrated that sources with a well-defined "V" and compact morphology almost universally host broad Hα, and, as such, our criteria will predominantly select LRDs once extended sources are removed.

3.1. Extremely Red Hα Emitter Selection

Here, we outline our selection of extremely red Hα emitters with a simple rest-frame color and equivalent width (EW) selection. Selecting on rest-frame colors has the advantage of ensuring that we are tracing the continuum shape without significant emission-line boosting, while still selecting for galaxies with strong Hα via an EW cut allows us to select for likely broad sources without requiring a determination of the line width at PRISM resolution for low signal-to-noise ratio (SNR) sources. These cuts are deliberately broad and will by definition include resolved extremely red galaxies (e.g., F. Gentile et al. 2024) and more "typical" reddened quasars (e.g., R. J. Assef et al. 2016) in addition to LRDs; we will then whittle this sample down to quantify what fraction of these sources meet LRD criteria.

First, we define a set of 0.07 μm width rest-frame filters which are designed to avoid strong emission and probe the rest-optical. The first filter, "*B*," spans 0.40–0.47 μm. The blue end was chosen to explicitly avoid the Balmer breaks, ensuring that we are selecting for all sources that are red independent of whether or not they have a break or V shape. The red end was chosen to terminate just blueward of Hβ. The second filter, "*R*," spans 0.67–0.74 μm, with the blue end motivated by starting redward of Hα and the red end set to keep the filter width identical to the *B* filter. We require that any galaxies we select have rest-frame wavelength coverage that spans the full range of our selection, effectively limiting us to galaxies at $z < 6.15$ due to the truncation of the red filter. We demonstrate these filters overlaid on the RUBIES-BLAGN-1, a broad-line emitting red source at $z = 3.1$ (B. Wang et al. 2025), in the left panel of Figure 1.

In addition to selecting on color, we also select based on the rest-frame EW of Hα+[N II]. To measure this EW, we fit for a power-law continuum between 0.58 and 0.73 μm, masking between 0.63 and 0.67 μm, and use this wavelength-dependent continuum to integrate the EW in the same 0.63–0.67 μm range. Again, while we do not explicitly select for broad lines, a high-EW selection can serve as a proxy that ensures that our selected sources could at least potentially host the highly luminous broad Hα that defines LRDs.

Using this color and EW and the magnitudes measured as specified in Section 2, we select all galaxies from the DJA that meet the following criteria:

1. $B - R > 0.95$.
2. EW(Hα) > 400 Å.
3. $m_{\rm F444W} < 26.5$.

The first two cuts are shown in the right panel of Figure 1, where we show the full DJA in this color plane and highlight this selection box in red, with literature samples of LRDs selected photometrically with V shapes (D. D. Kocevski et al. 2025) shown highlighted in orange, RUBIES-BLAGN-1 (B. Wang et al. 2025) shown as a purple star, and DJA/RUBIES sources shown in black and red, respectively. The color and EW cuts were motivated to include the vast majority of literature V shapes without explicitly selecting for any UV break. Because we do not explicitly select for compactness or incorporate any rest-UV information into our selection, we are effectively selecting extremely red, strong Hα emitters. The magnitude cut is motivated by the depth of the RUBIES PRISM spectroscopy (48 minutes exposure times), and corresponds to a median continuum SNR ~ 3 per pixel for a well-centered point source. In total, the selection yields 62 sources with extremely red colors and high-EW Hα.

Finally, we also attempt to quantify whether the sources in our sample are resolved. To do so, we take the ratio of the flux in a 0.″2 circular aperture to the flux in a 0.″1 aperture for the NIRCam/F444W imaging. We use the empirically derived point-spread function models for the F444W band from the UNCOVER survey (PIs: R. Bezanson and I. Labbe; R. Bezanson et al. 2024; J. R. Weaver et al. 2024) to estimate that this ratio should be ∼1.5 for unresolved sources. Accounting for the varying dithering strategies and depths of the imaging used here in addition to the centering of the slits on sources, we conservatively consider sources with $f(\frac{0.''2}{0.''1}) > 1.8$ to be resolved, and note that this distinction is purely qualitative and does not enter rigorously into our analysis.

A full gallery of the spectra of these extremely red Hα emitters is shown in Figure 2, with insets showing the F444W images of the sources. Sources with $f(\frac{0.''2}{0.''1}) > 1.8$ are highlighted in gray. While we did not explicitly select for compactness, the vast majority of the sources in this sample do indeed appear extremely compact. For each source, we mark H_∞ (0.3645 μm) with a dashed line to illustrate that many galaxies exhibit strong inflections in their spectral slope at this specific wavelength. In the next section, we will quantify that impression.

3.2. Determining Spectral Slope Inflection Strength and Location

The primary goal of this work is to study the continuum shape of spectroscopically confirmed extremely red Hα emitters. We aim to determine whether the finding that some specific LRD systems have strong inflections that resemble Balmer breaks (e.g., B. Wang et al. 2024b, 2025; Y. Ma et al. 2025; I. Labbe et al. 2025) is a feature of the population of these objects as a whole. As such, we require a metric that satisfies the following conditions:

1. The metric can determine whether sources exhibit a sharp change in slope.

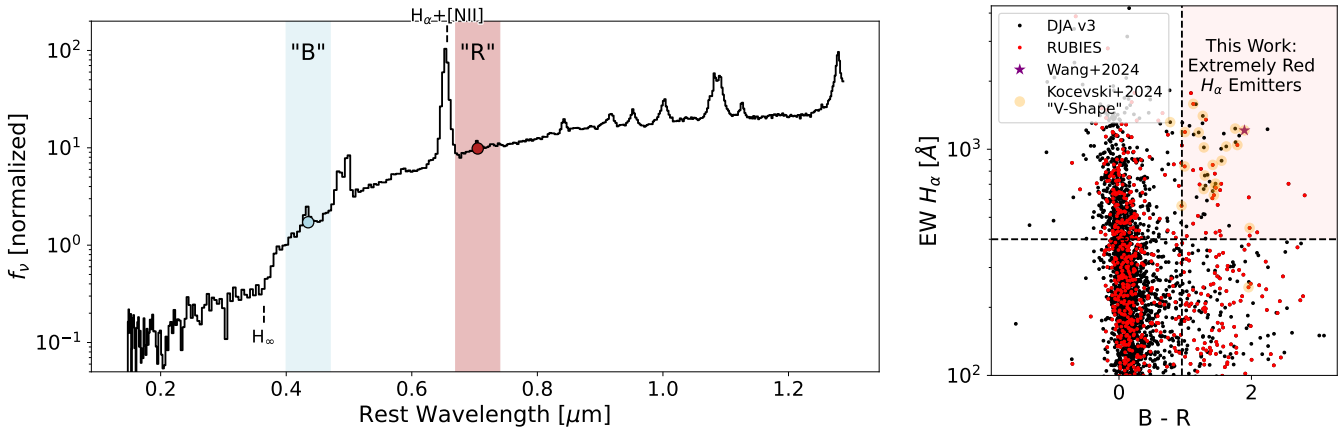

Figure 1. A demonstration of our color-EW selection of galaxies with LRD-like rest-frame colors. Left: the spectrum of RUBIES-BLAGN-1 (B. Wang et al. 2025), with synthetic rest-frame "*B*" and "*R*" filters (chosen to avoid strong emission lines) labeled as blue and red, respectively. The Balmer limit, H_∞, and Hα+[N II] are labeled. Right: $B-R$ versus EW Hα for the entire RUBIES/DJA PRISM sample with $m_{\rm F444W} < 26.5$. Sources from the RUBIES Cycle 2 program are shown as red, and all other sources from the DJA are shown as black. The top-right box contains extremely red sources with strong Hα emission, capturing sources that were selected photometrically to have a V shape in D. D. Kocevski et al. (2025, orange), and the RUBIES-BLAGN-1 (highlighted as a purple star).

2. The metric can, at least approximately, determine where that change in slope occurs.
3. The metric remains agnostic to the physics of that inflection, meaning the change in slope can occur at any wavelength.

To that end, we fit the spectra that fall into our extremely red Hα-emitting selection with a simple broken power-law model taking the following form:

$$f_\nu \propto \begin{cases} \lambda^{k_{\rm blue}} \ (\lambda < \lambda_{\rm break}) \\ \lambda^{k_{\rm red}} \ (\lambda > \lambda_{\rm break}) \end{cases} . \quad (1)$$

This model is quite similar to the rolling bandpass method employed by D. D. Kocevski et al. (2025) in identifying LRDs from photometry, making it a valuable tool for flagging galaxies where such a V shape occurs, with the additional feature of placing some constraints on the location of that inflection point by not enforcing that the inflection occurs at H_∞. We use `emcee` (D. Foreman-Mackey et al. 2013) to fit this model to all of our extremely red Hα emitters in the range $0.15\,\mu{\rm m} < \lambda < 0.6\,\mu{\rm m}$ (deliberately choosing a wide wavelength range to remain agnostic to the specific inflection location), with the normalization ($a > 0$), the break wavelength ($\lambda_{\rm break} \in [0.25, 0.5]$), and two power-law indices ($k_{\rm blue}$ and $k_{\rm red} \in [-10, 10]$) as free parameters. In order to account for model mismatch between this simple broken power law, the true shape of these systems, and the flux calibration being uncertain, we apply "grease" to the models in two ways. The first is enforcing a floor in the SNR of 20. Second, we fit for a free white-noise error inflation term ($\in$[0.1, 5]) that is penalized in our likelihood function. We mask the 0.005 μm region on either side of all strong emission features in this wavelength range, including [O II], Hδ, Hγ, and He I in these fits, and evaluate likelihood in $\log(f_\nu)$ when comparing to the model, effectively masking all negative fluxes.

In Figure 2, we show the median (red line) and 1σ (shaded region) constraints for all our fits. The gallery is sorted in descending order of median constraints on $k_{\rm red} - k_{\rm blue}$ (which we refer to as the inflection strength). Sources which are consistent at the 2σ level with $k_{\rm red} - k_{\rm blue} > 0$ have frames outlined in red, sources which are consistent with $k_{\rm red} - k_{\rm blue} > 0$ at the 1σ level have frames outlined in green, and all other sources have frames outlined in blue. In each panel, we mark 0.3645 μm, the limit of the Balmer series, as a dashed line for illustrative purposes. Visual inspection of the well-determined red inflection sample suggests that the majority, if not all, of the strong changes in slope occur quite near to this wavelength. However, it is striking that despite this, there is a wide variety of shapes of these changes in slope, ranging from transitions where a weak UV suddenly jumps (e.g., UNCOVER-45924; see also I. Labbe et al. 2025) to strong UV components that quickly change slopes without necessarily "breaking" (e.g., JADES-28074 and 6585-58018). We also note that there appears to be a distinction between the concavity of the red continuum in these two classes of objects, with the former tending to become shallower redward of the inflection point and the latter better resembling an already shallow power law. The results of this fitting are also shown in Table 1 in the same order (left to right) as they appear in Figure 2. For posterity, we also report the Balmer break strength as measured in B. Wang et al. (2024b), the ratio of the mean flux density (in f_ν) in the bandpasses $\lambda = 4000$–4100 Å and $\lambda = 3600$–3700 Å.

In order to explore this quantitatively, in Figure 3 we plot the inflection strength versus the wavelength of the break, with our well-determined (>2σ) sample highlighted as red points. We additionally highlight as solid sources where the break location is considered to be "well determined," with $\lambda_{\rm break,84} - \lambda_{\rm break,16} < 750$ Å. We note only sources with $k_{\rm red} - k_{\rm blue} > 0$ at the 2σ level ever meet this well-determined inflection criteria. However, given that the double power law is a poor descriptor of the actual shape of some of these sharp breaks (see, e.g., RUBIES-uds-40579 and UNCOVER-45924), it is not surprising that the break location we measure does not perfectly align with H_∞. To test this, we fit our double power-law model to a range of galaxy-only models—drawn from a grid of $t_{\rm age} = [0.1, 0.4]$ Gyr, $\tau_V = [2$–$4]$ (assuming a M. Kriek & C. Conroy 2013 dust law with a steep dust index of -1; see Y. Ma et al. 2025) and $f_{\rm scatter} = [0.5\%$–$2\%]$ (see Section 4.3)—with strong Balmer breaks, and find that fits to breaks that are purely stellar in origin span a range of $2.5 \gtrsim k_{\rm red} - k_{\rm blue} \gtrsim 6$ and $0.3 \gtrsim \lambda_{\rm break} \gtrsim 0.35$. Visual inspection of the population with strong changes in spectral slope confirms that the location of the inflection point itself is quite uniform. We acknowledge two sources with well-determined breaks that do not fall into this region; in both these sources (1433-1045

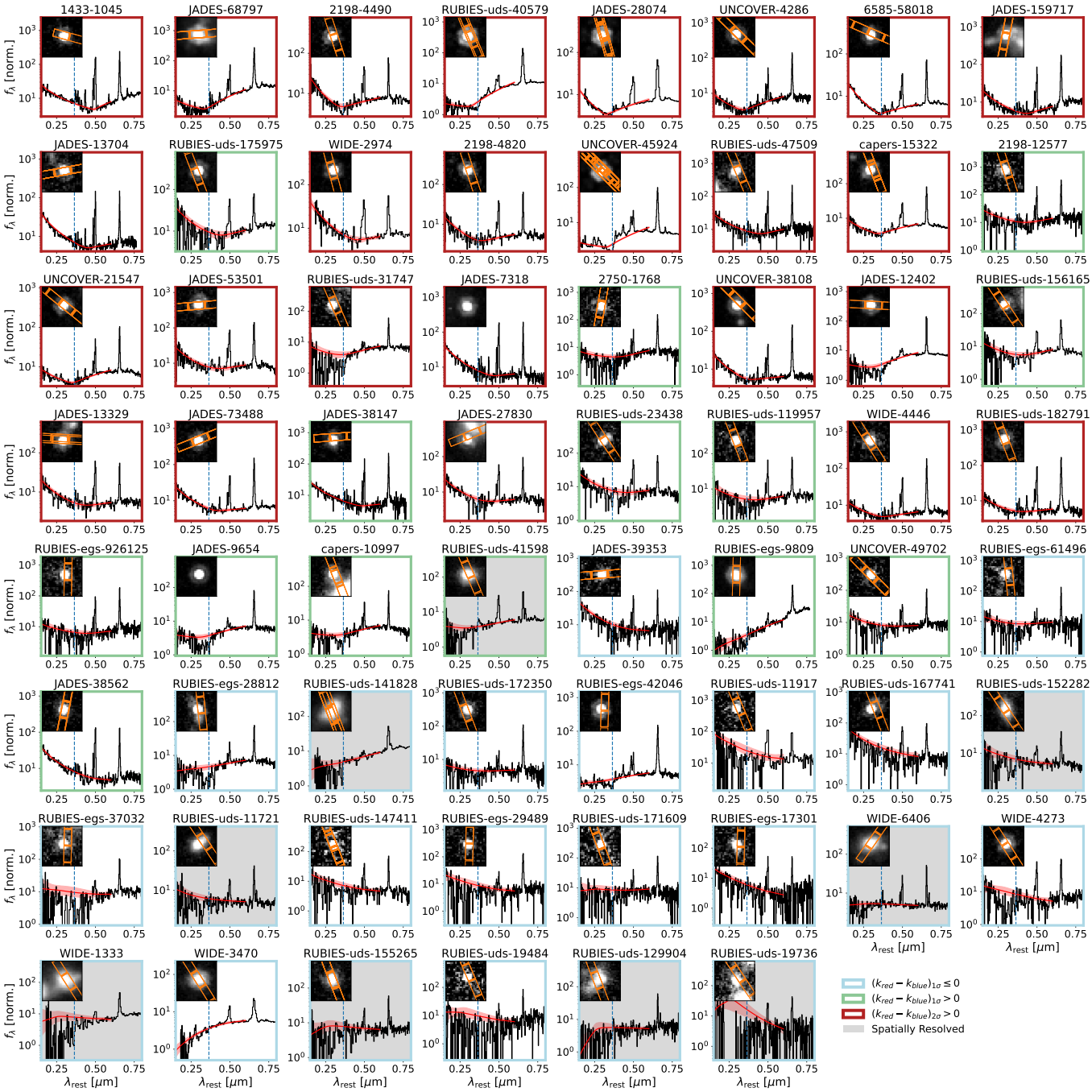

Figure 2. PRISM spectra of red, Hα-strong galaxies from the DJA are shown in black, with broken power-law fits to the emission-masked spectra shown in red. The spectra are ordered, from top to bottom, by the 50th percentile constraint on the difference between the red and blue power-law indices, from reddest to bluest. Sources are outlined based on the constraints on $k_{\rm red} - k_{\rm blue}$, with >0 at the 2σ level shown in red, >0 at the 1σ level shown in green, and $\leqslant 0$ at at the 1σ level shown in blue. Sources with a gray background have $f(0\farcs2/0\farcs1) > 1.8$, which we consider to be resolved. The sources which favor a strong change in slope all change slope at an extremely similar wavelength, close to 0.3645 μm (H_∞).

and JADES-13704), there is strong Balmer line emission and a feature that resembles a Balmer jump (e.g., H. Katz et al. 2025) directly before the slope becomes red, suggesting that these sources also seem to share the clear association with a transition associated with the Balmer series. In these sources, there may indeed be a secondary component of a nebular emission region (perhaps driven by vigorous star formation in a host galaxy or a high fraction of UV escape from an AGN that is atypical in LRDs) that dominates over the red continuum. High-resolution spectroscopy of the Balmer series in these sources could help to resolve how these sources differ from the rest of the population where such emission is not seen.

Finally, we note that the sample where no inflection location is determined is highly heterogeneous. Visual inspection of these sources reveals that some may indeed have changes in slope that are washed out by the low continuum SNR (e.g., RUBIES-egs-37032); many of these sources also appear to have slits that are poorly aligned with sources, making recovery of their rest-frame UV slopes difficult. Others, mostly among the resolved sample, clearly resemble dusty star-forming galaxies. It is noteworthy that these are among the

Table 1
All Extremely Red ($B - R > 0.95$) Hα Emitters (Rest-frame EW > 400 Å) from the RUBIES Survey or Public PRISM Data

Program	ID[a]	R.A.	Decl.	z	$m_{\rm F444W}$	$B-R$	$\rm EW_{H\alpha}$ (Å)	$f(\frac{0.''2}{0.''1})$	$\lambda_{\rm break}$ (μm)	Δk	Break Strength
1433	1045	06:47:44.02	+70:11:53.76	4.5295	24.5	1.81	1149	1.39	$0.49 \pm^{0.01}_{0.01}$	$4.0 \pm^{0.8}_{0.8}$	0.86 ± 0.01
JADES	68797	12:36:54.99	+62:08:46.28	5.0352	22.6	2.24	1226	1.54	$0.34 \pm^{0.02}_{0.02}$	$3.7 \pm^{0.5}_{0.5}$	2.51 ± 0.03
2198	4490	03:32:9.85	−27:51:16.14	3.7011	25.4	1.27	517	1.36	$0.34 \pm^{0.03}_{0.04}$	$3.3 \pm^{0.6}_{0.7}$	2.3 ± 0.02
RUBIES	uds-40579	02:16:58.61	−05:14:45.14	3.1124	22.3	1.89	1212	1.35	$0.32 \pm^{0.02}_{0.02}$	$3.3 \pm^{0.6}_{0.6}$	3.31 ± 0.02
JADES	28074	12:36:15.5	+62:16:25.73	2.2723	22.1	1.54	1005	1.32	$0.32 \pm^{0.01}_{0.01}$	$3.2 \pm^{0.3}_{0.3}$	1.58 ± 0.01
UNCOVER	4286	00:14:28.61	−30:25:23.77	5.8353	25.1	1.55	890	1.4	$0.34 \pm^{0.02}_{0.02}$	$3.0 \pm^{0.5}_{0.5}$	1.26 ± 0.01
6585	58018	10:00:34.67	+02:20:39.81	3.9278	24.3	1.46	705	1.35	$0.35 \pm^{0.01}_{0.01}$	$3.0 \pm^{0.2}_{0.2}$	1.43 ± 0.01
JADES	159717	03:32:23.41	−27:54:4.54	5.0768	24.4	1.75	1234	1.53	$0.43 \pm^{0.03}_{0.05}$	$3.0 \pm^{0.7}_{0.6}$	1.08 ± 0.02
JADES	13704	03:32:30.37	−27:49:5.13	5.9296	26.2	1.3	765	1.4	$0.44 \pm^{0.03}_{0.03}$	$2.9 \pm^{0.8}_{0.6}$	1.17 ± 0.01
RUBIES	uds-175975	02:16:50.49	−05:05:55.45	2.9451	24.3	1.97	449	1.34	$0.43 \pm^{0.05}_{0.08}$	$2.8 \pm^{1.5}_{1.4}$	2.0 ± 0.03
WIDE	2974	14:20:30.42	+53:02:54.11	2.3231	24.8	1.41	653	1.34	$0.43 \pm^{0.04}_{0.06}$	$2.7 \pm^{1.1}_{1.0}$	0.83 ± 0.01
2198	4820	03:32:8.37	−27:51:7.89	3.7966	25.5	1.28	667	1.34	$0.37 \pm^{0.04}_{0.04}$	$2.6 \pm^{0.6}_{0.7}$	1.11 ± 0.02
UNCOVER	45924	00:14:20.34	−30:20:37.06	4.4668	22.5	1.06	1270	1.35	$0.33 \pm^{0.01}_{0.01}$	$2.6 \pm^{0.2}_{0.2}$	3.92 ± 0.01
RUBIES	uds-47509	02:17:3.5	−05:13:57.31	5.6752	25.0	1.42	853	1.49	$0.44 \pm^{0.04}_{0.06}$	$2.6 \pm^{1.2}_{1.0}$	1.14 ± 0.03
capers	15322	02:17:40.76	−05:09:15.22	3.709	24.3	1.34	771	1.42	$0.34 \pm^{0.02}_{0.02}$	$2.5 \pm^{0.4}_{0.4}$	1.64 ± 0.01
2198	12577	03:32:11.63	−27:48:54.51	5.232	25.5	1.76	1075	1.32	$0.42 \pm^{0.05}_{0.07}$	$2.4 \pm^{1.2}_{1.2}$	1.48 ± 0.02
UNCOVER	21547	00:14:12.2	−30:24:23.75	5.0544	24.6	1.44	681	1.39	$0.35 \pm^{0.01}_{0.01}$	$2.4 \pm^{0.3}_{0.3}$	1.68 ± 0.01
JADES	53501	12:37:10.81	+62:11:36.86	3.4283	25.0	1.29	1124	1.33	$0.4 \pm^{0.06}_{0.07}$	$2.4 \pm^{0.9}_{0.9}$	1.47 ± 0.02
RUBIES	uds-31747	02:16:53.7	−05:15:36.88	4.1305	25.1	1.54	416	1.39	$0.36 \pm^{0.06}_{0.05}$	$2.4 \pm^{0.9}_{1.0}$	1.9 ± 0.02
JADES	7318	03:32:39.05	−27:52:23.26	5.5507	24.0	0.96	1311	1.52	$0.45 \pm^{0.03}_{0.07}$	$2.4 \pm^{1.1}_{0.9}$	1.36 ± 0.08
2750	1768	14:19:42.18	+52:56:44.38	5.0946	26.1	1.62	1029	1.35	$0.41 \pm^{0.06}_{0.07}$	$2.4 \pm^{1.1}_{1.1}$	2.02 ± 0.01
UNCOVER	38108	00:14:7.2	−30:21:28.85	4.962	25.0	1.2	1187	1.35	$0.37 \pm^{0.04}_{0.03}$	$2.3 \pm^{0.5}_{0.5}$	1.49 ± 0.01
JADES	12402	03:32:31.84	−27:45:55.74	3.1965	24.3	1.58	1173	1.32	$0.32 \pm^{0.04}_{0.03}$	$2.2 \pm^{1.0}_{1.0}$	2.62 ± 0.02
RUBIES	uds-156165	02:18:0.12	−05:07:38.15	2.7685	24.6	1.53	660	1.34	$0.4 \pm^{0.06}_{0.06}$	$2.2 \pm^{1.2}_{1.2}$	1.68 ± 0.03
JADES	13329	03:32:33.37	−27:47:3.96	3.9441	25.5	1.29	515	1.45	$0.41 \pm^{0.06}_{0.07}$	$2.2 \pm^{1.0}_{0.9}$	1.3 ± 0.02
JADES	73488	12:36:47.38	+62:10:38.04	4.1304	25.3	1.26	1302	1.37	$0.4 \pm^{0.04}_{0.04}$	$2.2 \pm^{0.6}_{0.5}$	1.24 ± 0.01
JADES	38147	12:37:4.96	+62:08:54.3	5.8778	25.2	1.16	1582	1.39	$0.47 \pm^{0.02}_{0.06}$	$2.1 \pm^{1.4}_{1.2}$	1.06 ± 0.03
JADES	27830	12:37:1.07	+62:14:57.34	3.9386	24.5	1.31	691	1.64	$0.4 \pm^{0.06}_{0.06}$	$2.0 \pm^{1.0}_{0.9}$	2.0 ± 0.03
RUBIES	uds-23438	02:17:21.19	−05:16:51.22	3.6907	24.9	1.46	676	1.47	$0.42 \pm^{0.06}_{0.08}$	$2.0 \pm^{1.5}_{1.4}$	0.94 ± 0.03
RUBIES	uds-119957	02:17:4.54	−05:10:36.2	4.1504	25.6	1.54	703	1.3	$0.4 \pm^{0.07}_{0.07}$	$2.0 \pm^{1.2}_{1.3}$	1.16 ± 0.02
WIDE	4446	02:17:4.97	−05:13:3.62	4.6909	24.3	1.27	1404	1.39	$0.37 \pm^{0.04}_{0.04}$	$1.9 \pm^{0.5}_{0.5}$	1.58 ± 0.03
RUBIES	uds-182791	02:16:51.32	−05:05:13.38	4.7195	25.1	1.09	1771	1.4	$0.38 \pm^{0.07}_{0.06}$	$1.7 \pm^{0.7}_{0.6}$	1.07 ± 0.03
RUBIES	egs-926125	14:20:32.9	+52:59:18.79	5.284	25.5	1.79	1044	1.37	$0.42 \pm^{0.05}_{0.09}$	$1.6 \pm^{1.5}_{1.5}$	0.7 ± 0.02
JADES	9654	03:32:21.35	−27:44:17.51	4.8245	25.0	1.37	719	1.36	$0.33 \pm^{0.06}_{0.04}$	$1.5 \pm^{0.8}_{0.9}$	3.23 ± 0.04
capers	10997	02:17:41.83	−05:08:11.43	5.1587	24.2	1.24	500	1.5	$0.35 \pm^{0.06}_{0.05}$	$1.5 \pm^{0.8}_{0.9}$	2.32 ± 0.02
RUBIES	uds-41598	02:16:55.31	−05:14:38.45	3.1934	23.1	1.52	435	1.92	$0.34 \pm^{0.09}_{0.06}$	$1.3 \pm^{0.9}_{0.9}$	1.0 ± 0.04
JADES	39353	12:37:10.55	+62:09:11.13	4.851	26.4	1.17	614	1.32	$0.42 \pm^{0.06}_{0.1}$	$1.3 \pm^{1.6}_{1.3}$	2.1 ± 0.03
RUBIES	egs-9809	14:20:4.15	+52:52:48.57	5.6844	23.5	2.8	626	1.51	$0.37 \pm^{0.08}_{0.07}$	$1.2 \pm^{1.2}_{1.1}$	2.76 ± 0.03
UNCOVER	49702	00:14:11.45	−30:20:1.33	4.8756	26.4	1.33	593	1.31	$0.39 \pm^{0.08}_{0.09}$	$1.2 \pm^{1.0}_{1.0}$	3.95 ± 0.01
RUBIES	egs-61496	14:19:53.39	+52:57:43.89	5.0764	26.1	1.43	627	1.42	$0.39 \pm^{0.08}_{0.09}$	$1.2 \pm^{1.5}_{1.6}$	1.57 ± 0.02
JADES	38562	03:32:32.61	−27:52:17.92	4.8263	26.1	1.13	1162	1.41	$0.45 \pm^{0.03}_{0.1}$	$1.2 \pm^{1.1}_{0.8}$	1.0 ± 0.02
RUBIES	egs-28812	14:19:41.8	+52:50:56.58	4.2195	24.8	1.41	607	1.42	$0.36 \pm^{0.08}_{0.07}$	$0.8 \pm^{1.1}_{1.3}$	2.46 ± 0.03
RUBIES	uds-141828	02:16:58.22	−05:08:50.33	2.3257	21.9	1.97	415	2.1	$0.38 \pm^{0.09}_{0.08}$	$0.8 \pm^{1.2}_{1.4}$	1.26 ± 0.03
RUBIES	uds-172350	02:17:28.55	−05:06:14.19	5.5777	24.8	1.0	1191	1.35	$0.37 \pm^{0.09}_{0.08}$	$0.7 \pm^{1.0}_{1.1}$	1.82 ± 0.03
RUBIES	egs-42046	14:19:10.89	+52:47:19.85	5.2702	23.5	1.12	1587	1.37	$0.33 \pm^{0.08}_{0.05}$	$0.6 \pm^{0.6}_{0.6}$	2.62 ± 0.03
RUBIES	uds-11917	02:17:4.38	−05:17:42.75	2.5909	26.1	1.49	568	1.34	$0.4 \pm^{0.08}_{0.12}$	$0.6 \pm^{3.0}_{2.9}$	0.47 ± 0.02
RUBIES	uds-167741	02:17:20.3	−05:06:36.97	4.1247	24.8	0.99	840	1.37	$0.41 \pm^{0.07}_{0.1}$	$0.5 \pm^{1.8}_{1.8}$	1.22 ± 0.06
RUBIES	uds-152282	02:18:1.44	−05:07:57.55	3.429	24.1	1.02	413	1.99	$0.38 \pm^{0.09}_{0.09}$	$0.4 \pm^{1.5}_{1.6}$	1.21 ± 0.09
RUBIES	egs-37032	14:19:23.85	+52:48:42.57	3.8467	25.4	1.96	613	1.38	$0.38 \pm^{0.09}_{0.1}$	$0.3 \pm^{2.6}_{2.7}$	4.57 ± 0.03
RUBIES	uds-11721	02:17:38.65	−05:18:2.81	3.9807	24.2	1.12	469	1.88	$0.38 \pm^{0.09}_{0.09}$	$0.3 \pm^{1.3}_{1.3}$	1.18 ± 0.04
RUBIES	uds-147411	02:17:26.57	−05:08:20.69	3.9638	26.4	1.12	808	1.37	$0.4 \pm^{0.08}_{0.11}$	$0.2 \pm^{1.8}_{1.8}$	1.37 ± 0.02
RUBIES	egs-29489	14:20:5.3	+52:55:14.83	4.5423	26.1	1.31	1351	1.31	$0.38 \pm^{0.09}_{0.1}$	$0.1 \pm^{2.0}_{2.0}$	1.92 ± 0.03
RUBIES	uds-171609	02:17:2.86	−05:06:18.74	5.2832	25.9	1.24	819	1.32	$0.37 \pm^{0.1}_{0.1}$	$0.1 \pm^{2.2}_{2.6}$	2.52 ± 0.03
RUBIES	egs-17301	14:19:57.0	+52:52:23.21	5.2246	26.1	1.22	699	1.56	$0.4 \pm^{0.07}_{0.12}$	$-0.1 \pm^{2.0}_{1.8}$	0.69 ± 0.03
WIDE	6406	12:37:6.27	+62:12:51.02	4.4108	24.2	1.02	456	2.19	$0.36 \pm^{0.1}_{0.08}$	$-0.3 \pm^{0.8}_{0.8}$	1.36 ± 0.05
WIDE	4273	02:17:27.24	−05:10:37.13	4.0611	24.5	1.28	1019	1.44	$0.37 \pm^{0.1}_{0.09}$	$-0.3 \pm^{1.8}_{1.9}$	1.39 ± 0.04

Table 1
(Continued)

Program	ID[a]	R.A.	Decl.	z	m_{F444W}	$B-R$	$EW_{H\alpha}$ (Å)	$f(\frac{0.''2}{0.''1})$	λ_{break} (μm)	Δk	Break Strength
WIDE	1333	02:17:51.61	−05:15:6.98	2.3115	22.3	1.66	459	2.02	$0.34\pm^{0.11}_{0.07}$	$-0.8\pm^{2.1}_{2.4}$	2.59 ± 0.04
WIDE	3470	02:18:2.97	−05:11:21.25	2.3045	22.4	1.31	403	1.57	$0.42\pm^{0.06}_{0.14}$	$-1.1\pm^{0.8}_{0.8}$	1.7 ± 0.03
RUBIES	uds-155265	02:17:5.19	−05:07:41.85	4.1073	25.4	1.31	427	1.89	$0.32\pm^{0.12}_{0.06}$	$-1.3\pm^{2.1}_{2.2}$	1.86 ± 0.04
RUBIES	uds-19484	02:16:55.78	−05:16:50.35	4.6627	26.2	2.09	429	1.59	$0.33\pm^{0.13}_{0.07}$	$-1.4\pm^{3.1}_{2.8}$	2.02 ± 0.03
RUBIES	uds-129904	02:17:6.27	−05:09:48.64	5.215	24.4	1.46	428	2.46	$0.28\pm^{0.11}_{0.03}$	$-3.5\pm^{2.8}_{3.1}$	1.35 ± 0.05
RUBIES	uds-19736	02:17:12.28	−05:17:16.14	4.8024	25.4	1.19	508	2.04	$0.27\pm^{0.13}_{0.02}$	$-4.8\pm^{4.7}_{4.2}$	1.89 ± 0.1

Notes. Sources are sorted by their median $k_{red}-k_{blue}$ (Δk), as determined by the fits described in Section 3.2.
[a] For RUBIES sources, we list both the field and ID, as fields do not have unique ID numbers. For JADES sources, the ID number represents the spectroscopic, not photometric, ID.

(This table is available in its entirety in machine-readable form in the online article.)

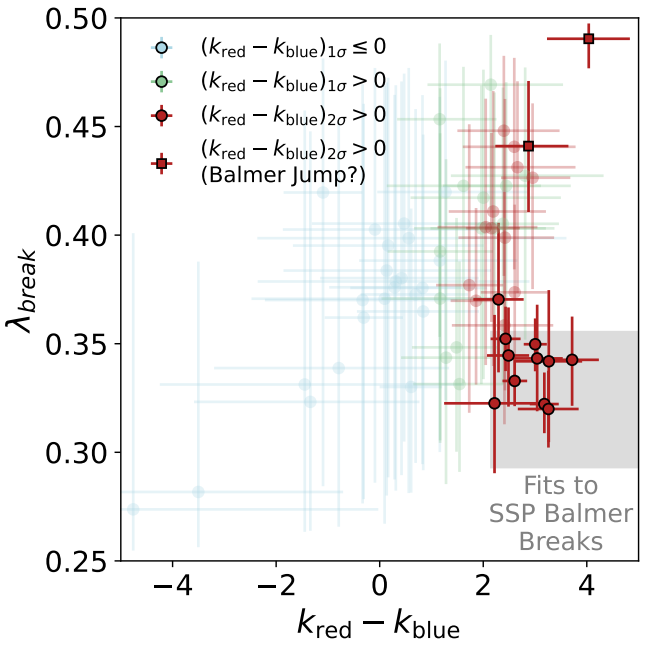

Figure 3. The results of the broken power-law fits to the red spectra, illustrated by showing the break wavelength versus the difference between the red and blue power-law indices. Sources with $k_{red}-k_{blue}>0$ at the 2σ level are colored red, those consistent with $k_{red}-k_{blue}>0$ at the 1σ level are colored green, and those consistent with no break are colored blue. Sources which have a well-determined break ($\lambda_{break,84}-\lambda_{break,16}<750$ Å) are shown as solid points, and all other sources are shown with transparency. The shaded gray region shows the range of $k_{red}-k_{blue}$ and λ_{break} that comes from applying this model to PRISM models of dusty poststarburst galaxies (with some scattered light; see Section 4.3). All of the galaxies with a preference for a strong change in slope are fit with a break that occurs near 0.3645 μm, the Balmer break, at a very similar wavelength to the one returned by model fits to simple stellar populations.

only sources that appear to have prominent [S II] emission, suggesting a significantly different ionizing mechanism (and potentially metallicity) to the unresolved V-shaped sources. Additionally, some number of these sources appear to be completely unresolved and have extremely red shapes but lack a strong UV component, resembling typical reddened quasars (e.g., E. Glikman et al. 2012; M. Banerji et al. 2015).

Sources with strong red changes in slope are essentially all unresolved in their F444W imaging. As such, these sources meet the V-shaped, compact LRD criteria employed in the literature (e.g., V. Kokorev et al. 2023; J. E. Greene et al. 2024; D. D. Kocevski et al. 2025; I. Labbe et al. 2025), and we make the empirical statement that sources in our sample with well-determined changes in spectral slope are V-shaped LRDs, and that LRD inflection points consistently occur at 3645 Å, the Balmer limit.

4. Why Are Changes in Spectral Slopes among LRDs Associated with the Balmer Limit?

In the previous section, we demonstrated that a significant portion (25/62) of extremely red galaxies with high-Hα EWs have strong changes in spectral slope (measured at the 2σ level) that consistently occur around ∼3645 Å. This likely represents a lower limit on the true fraction of extremely red Hα emitters with such inflection points, as our stringent criteria for a significant change in slope would make weak changes hard to detect in low-SNR sources or sources with fainter intrinsic UV continuum (many of these sources appear in our 1σ sample). Models have explained this inflection point using a variety of prescriptions, including a reddened quasar with a UV dominated by scattered light (e.g., H. B. Akins et al. 2025; G. Barro et al. 2024; L. J. Furtak et al. 2024; J. E. Greene et al. 2024; I. Labbe et al. 2025), a reddened AGN with a UV dominated by stellar continuum (e.g., J. E. Greene et al. 2024; B. Wang et al. 2024b, 2025; Y. Ma et al. 2025), a continuum fully dominated by stellar light (e.g, H. B. Akins et al. 2023; I. Labbé et al. 2023; C. C. Williams et al. 2024), a gray dust law (Z. Li et al. 2025), or absorption from a nonstellar source of $n=2$ hydrogen (K. Inayoshi & R. Maiolino 2025). In this section, we use a set of toy models to test whether these scenarios are at odds with our finding that the inflection point in the V shape occurs at a consistent wavelength.

In order to do so, we construct an oversampled stack of the 19 sources that are fit with strong changes in slope (excluding the one resolved source with a well-determined inflection point). We interpolate each rest-frame spectrum onto a grid spanning 0.2 μm–0.7 μm in bins of 0.001 μm after normalizing the median flux density in the 100 Å window around H_∞ to be 1. We then take the median flux of all sources in each supersampled pixel, weighting each galaxy equally, and we also measure the standard error in the median of each of these pixels.

We show this stack in Figure 4 in red, showing the standard error in the median as a shaded region. For illustrative purposes, we also show the stack of the unresolved sources that are

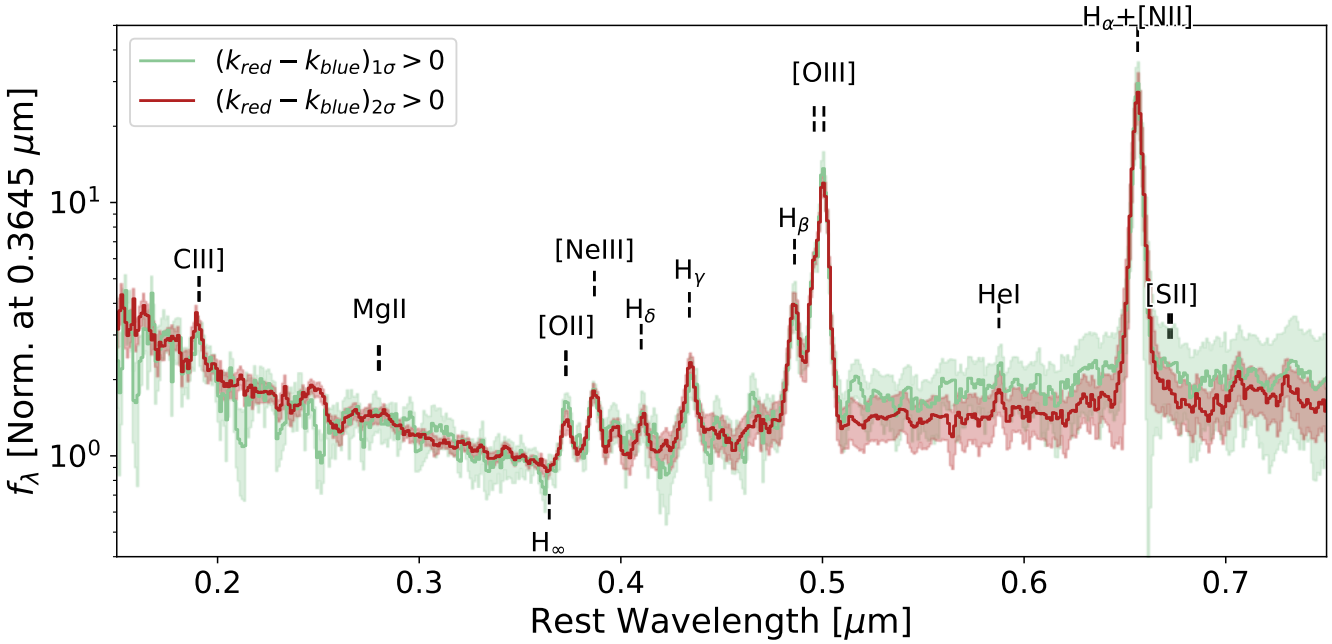

Figure 4. Median stacks of the 2σ (red) and 1σ (green) samples that are unresolved (see Figure 3). Shaded regions denote the error in the median. The sources with well-constrained red changes in slope show a strong preference for an inflection at and around 0.3645 μm, H_{∞}. The stack of sources with less well constrained changes in slope still exhibit a similar shape at H_{∞}. Key emission features are labeled.

consistent with changes in slope at the 1σ level in green. The stack of LRDs shows an extremely strong preference for an abrupt jump right at H_{∞}, with a characteristically blue slope blueward of the Balmer limit and a wider range of red-end slopes. The 1σ stack appears similar, indicating again that a significant fraction of the sources in that sample have common inflection points. Both stacks show strong Balmer series emission, in addition to C III], [O II], [O III], [Ne III], and He I.

In this work, we are primarily concerned with the physical origin of the strong changes in slope among LRDs. Based on our analysis, it is clear that any model which can explain these spectral inflection points must consistently produce a sharp change in slope at H_{∞} without invoking an extremely specific combination of reddening and fractional contribution of two components, and result in an SED that is red enough to fall into our $B - R$ color selection.

In the following sections, we employ a set of toy models to assess whether LRD models proposed in the literature can explain the sharp transitions seen in a large fraction of extremely red galaxies. We stress that we are not fitting any models in this section to the stacked data. Instead, we use the models to illustrate what types of models can satisfy the above criteria by comparing to the shape of the stack at and around 3645 Å. As a general rule, any model that is plotted with a solid line meets the $B - R > 0.95$ criterion for "extremely red" outlined in Section 3, while models that do not are plotted as dashed lines. All stellar population models are generated with Flexible Stellar Population Synthesis (C. Conroy et al. 2009; C. Conroy & J. E. Gunn 2010) with nebular emission turned off, and all AGN models are generated using the M. J. Temple et al. (2021) model.

4.1. An Inflection Arising from the Transition between Reddened AGN Continuum and Scattered Light

Because of their broad lines and compact morphologies, it has been suggested that LRDs are hosts to obscured AGN, with their continuum shape dominated by a reddened accretion disk (e.g., G. Barro et al. 2024; L. J. Furtak et al. 2024; J. E. Greene et al. 2024; I. Labbe et al. 2025). In this model, the V shape of the spectrum results from an intersection between a reddened AGN continuum and a significantly smaller scattered-light component that has the spectrum of the unreddened AGN (L. J. Furtak et al. 2023; J. E. Greene et al. 2024). Many dusty quasars, both in the local Universe (S. Veilleux et al. 2013) and at high redshift (E. Glikman et al. 2012; R. J. Assef et al. 2016; F. Hamann et al. 2017), are well described by such a model.

To model the two-component AGN-only model, we follow H. B. Akins et al. (2025) and Y. Ma et al. (2025) and assume that the intrinsic AGN SED follows the empirically measured M. J. Temple et al. (2021) continuum shape derived from type 1 quasars at $0 < z < 5$. We assume that some fraction of this light is attenuated following a S. Noll et al. (2009) and M. Kriek & C. Conroy (2013) dust law, with a dust index that controls the offset of the curve relative to the D. Calzetti (1997) dust law and parametrizes the UV bump, δ, and a normalization τ_V, and that the rest of the light is not attenuated. The dust law takes the form

$$k(\lambda) = \begin{cases} 1.17(-1.857 + 1.04\lambda^{-1}) + 1.78 & (\lambda > 6300) \\ 1.17(-2.156 + 1.509\lambda^{-1} - 0.198\lambda^{-2} & \\ \quad +0.011\lambda^{-3}) + 1.78 & (\lambda \leqslant 6300) \end{cases}, \tag{2}$$

$$D(\lambda) = \frac{(0.85 - 1.9\Delta_\lambda)(\lambda\Delta_\lambda)^2}{(\lambda^2 - \lambda_{\rm UVB}^2)^2 + (\lambda\Delta_\lambda)^2}, \tag{3}$$

$$\tau(\lambda) = \frac{\tau_V}{4.05}\left(\frac{k(\lambda)}{0.44} + D(\lambda)\right)\left(\frac{\lambda}{5500}\right)^{\delta}. \tag{4}$$

In Figure 5(a), we show the stack of our LRD sample with strong red changes in slope in red, along with a set of models generated using one intrinsic AGN model under a range of

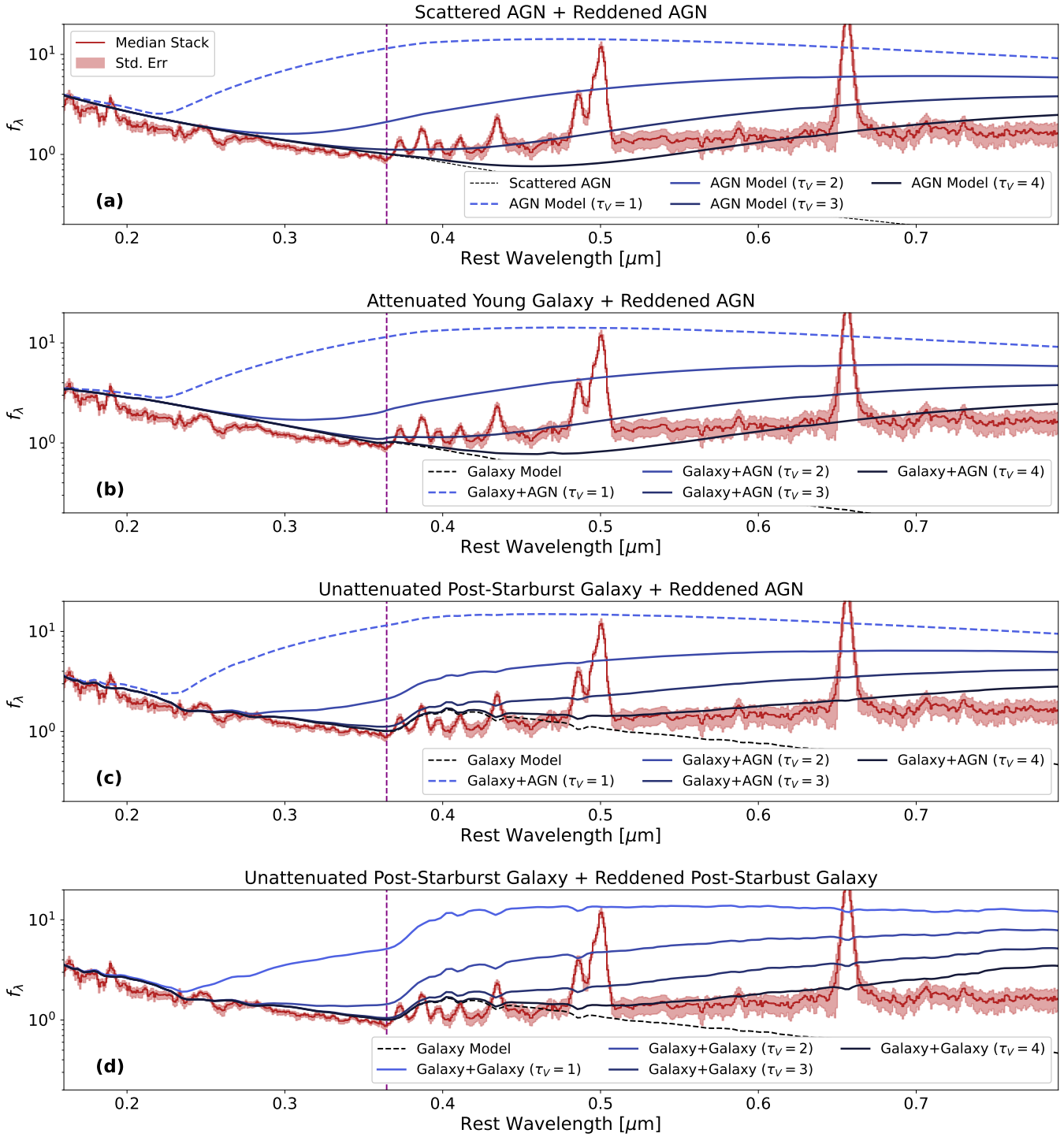

Figure 5. A median stack of the spectra (red) of all spectra with high-confidence slope changes. On the top, we show four AGN-AGN models, which are generated by scattering 1% of the light from an intrinsic AGN continuum model (M. J. Temple et al. 2021, blue dashed line) and attenuating the remainder of the light by the indicated τ_V using a M. Kriek & C. Conroy (2013) dust law with a dust index of -1. The AGN models are normalized so that the contribution from the scattered component is 1 at 3645 Å, which is also where the spectra in the stack are normalized. In the next two rows, we show the same set of AGN models, but replacing the UV component with an $\tau_v \sim 0.75$ star-forming galaxy (row 2) and dust-free post-starburst galaxy (row 3) normalized to the UV. Models that meet the $B - R > 0.95$ cut are shown as solid lines, and models that do not are shown as dashed lines. Finally, we show a two-component galaxy model with the same unreddened poststarburst as the previous row, with the reddened AGN is replaced by the same stellar population undergoing varying reddening. In all cases, models *can* produce a change in slope at 3645 Å, but only with a very specific configuration of galaxy age, galaxy/AGN flux balance, and reddening. It is unlikely that any two-component model where the two components originate from different physical origins would result in this uniform inflection location.

attenuation assumptions. All models are set to $f_{\rm scatter} = 1\%$ and are normalized so that the scattered-light component is equal to our stack at 3645 Å. This scattered-light component is shown as a dotted black line. We then show a range of four AGN attenuation models, with the remaining 99% of the light subjected to dust screens of $\tau_V = 1$, 2, 3, and 4. For all these models, we set the dust index (see M. Kriek & C. Conroy 2013) to -1, which is steeper than any commonly

used dust law but is required to produce a red continuum from dust attenuation that falls off steeply enough around H_∞ to match the observed SED shape of LRDs (see Y. Ma et al. 2025, for more discussion).

Even under the assumption of an extremely steep dust law, this model does not prove to be a good description of the observed spectral shapes of LRDs. First, it is difficult for the shape of the inflection to be steep enough to appear as an abrupt jump in the spectrum; this is because the intersection of the scattered and extincted AGN power laws results in a smooth transition between the two components. But, perhaps even more importantly, this model fails to meet our criteria for describing the shape of LRDs because there is no reason that these weak changes in slope should consistently occur at some preferred wavelength. Indeed, the models that would result in a system that is red enough to meet our $B-R$ selection ($\tau_V = 2$, 3, and 4, similar to the range of attenuation found to result in observed LRD colors in M. Volonteri et al. 2025) show inflection points that range from rest-frame $\sim$0.25 μm out to $\sim$0.4 μm. And while for any given τ_V there exists a scattering fraction that could combine to locate the inflection right around 3645 Å, it would be extremely unlikely for all observed systems to be configured precisely such that this change in slope occurs at the same location. We note that this claim is not unique to the assumed M. J. Temple et al. (2021) AGN model: Any AGN model with a smooth continuum that does not feature any intrinsic inflection points (e.g., A. Kubota & C. Done 2018) would fail to replicate the observed LRD spectral shape.

It has also been suggested that a "gray" dust law such as that of the Orion Nebula (J. A. Baldwin et al. 1991), where the attenuation curve is approximately flat from the UV to 4000 Å, could be responsible for producing the V shape in LRDs (Z. Li et al. 2025). While this model performs well enough on photometry to broadly produce an LRD-like shape, Y. Ma et al. (2025) demonstrate that it cannot produce a sharp enough "V" to fit the spectroscopic shape in LRDs with a strong inflection at the Balmer limit; and the same would be true in many of the sources in this work, especially those with the strongest inflections in slope that occur abruptly. Thus, we conclude similarly that the ubiquity of a specific wavelength of transition in many LRDs as opposed to a slowly rolling transition disfavors this model.

Thus, we claim that it is extremely unlikely that the typical spectra of LRDs with strong changes in spectral slope can be the result of a two-component AGN model that produces these changes via the intersection of a scattered and an attenuated component. Even putting aside the issue of the steepness of the red-end slope (which could result from some different intrinsic AGN shape or dust grain size distributions that result in an even steeper dust law; see Y. Ma et al. 2025) and the issues related to the deficiency of X-ray (H. B. Akins et al. 2025; T. T. Ananna et al. 2024; L. J. Furtak et al. 2024; R. Maiolino et al. 2025; M. Yue et al. 2024) and rest-frame 3–4 μm emission (H. B. Akins et al. 2025; C. C. Williams et al. 2024; B. Wang et al. 2025), emission typically seen in AGN, the consistency and sharpness of the inflection point is highly unlikely to result from any model that invokes the intersection of two components with no intrinsic changes in slope to explain the observed spectral shapes.

4.2. An Inflection Arising from the Transition between a Reddened AGN Continuum and Stellar Continuum

Because the model of a reddened AGN continuum with a scattered-light component fails to meet the criteria necessary to describe observed LRD spectra, we now turn to another commonly invoked model where the LRD spectral shape is caused by the intersection between a UV component that is dominated by galaxy light and a reddened AGN. This model has been shown to successfully replicate the continuum shape of spectroscopically confirmed LRDs with broad lines (B. Wang et al. 2024b, 2025; Y. Ma et al. 2025), though the exact range of the contribution of galaxy and AGN light at a given wavelength—as well as the age, reddening, and mass of the underlying stellar component—can be highly uncertain.

We test two versions of this model. In the first, the underlying stellar population is young and moderately dusty (simulated as a 2 Myr-old simple stellar population embedded in $\tau_V = 0.25$). We treat the reddened quasar models identically to in Section 4.1. In Figure 5(b), we show this model for the same range of AGN attenuation ($\tau_V = 1$–4) as compared to our 2σ stack. As expected, this model fails to capture the true shape of LRDs almost identically to the model where the UV results from an unobscured AGN: because there is no intrinsic inflection point in either of the intersecting models. The change in slope can occur at any wavelength, and the resultant breaks are not nearly as sharp as is observed in the stack.

It has therefore been suggested instead that the underlying stellar population that is producing the UV emission must be evolved enough that it lacks O and B stars, resulting in a Balmer break (B. Wang et al. 2024b, 2025; Y. Ma et al. 2025), with the reddened AGN component picking up just redward of the Balmer break to produce the observed red continuum. Thus, we test a second implementation of the galaxy+AGN model by replacing the previous young simple stellar population instead with a dust-free 100 Myr-old simple stellar population with light dominated by A stars. In Figure 5(c), we show this model compared to our stack, again with the same range of reddened quasar models. In contrast with the previous two models, this model is fully capable of replicating the UV continuum, break, and red continuum for the proper configuration of AGN attenuation and luminosity relative to the underlying stellar population. This model does suffer from the specificity required in this balance between AGN and galaxy light, but that may be partly due to selection: Sources where the reddened AGN is totally dominant over the host galaxy would not have any significant UV component and would not be fit with any breaks in our model. It is therefore feasible, at least qualitatively, that V-shaped LRDs could result from the intersection of an evolved stellar population and a reddened AGN.

4.3. An Inflection Resulting from a Dusty Evolved Stellar Population with Some UV Escape

It has also been suggested that the entire continuum in LRDs can be ascribed to starlight, with standard SED modeling approaches adequately capturing the UV+optical with a young unattenuated population and the red end captured by dust-obscured stars (e.g., H. B. Akins et al. 2023, 2025; I. Labbé et al. 2023; C. C. Williams et al. 2024; B. Wang et al. 2024b). These models solve a number of problems present in the galaxy+AGN model, including the lack of X-ray detections

(H. B. Akins et al. 2025; T. T. Ananna et al. 2024; L. J. Furtak et al. 2024; R. Maiolino et al. 2025; M. Yue et al. 2024) and flat mid-IR (MIR) SEDs (e.g., H. B. Akins et al. 2025; B. Wang et al. 2025; C. C. Williams et al. 2024). It has also been suggested that the width of the broad Balmer emission in these models is fully consistent with the compact sizes of these sources and does not need to originate from an accretion disk (J. F. W. Baggen et al. 2024), lending credence to the idea that these systems could simply be the early-forming cores of present-day elliptical galaxies (J. F. W. Baggen et al. 2023). While the source of ionizing radiation (e.g., Y. Ma et al. 2025) and the dust geometry (LRD broad lines are consistent with significant attenuation, but the narrow lines are not; see M. Brooks et al. 2025) for the Balmer emission presents an issue for such models, they merit exploration due to the natural connection between a break at H_∞ and evolved stellar populations.

In Figure 5(d), we demonstrate that this model can, similarly to the galaxy+AGN model, produce shapes that are broadly consistent with our LRD stack without necessitating significant tuning, even under the simplified assumption that the galaxy is a simple stellar population, where the UV originates from 1% of stars that are unattenuated and the red continuum now comes from the remaining 99% of galaxy light that sees a dust screen. Thus, it is indeed possible that the typical LRD spectral shape results from starlight alone, provided there is enough unattenuated light to produce the observed UV+break and that the reddened component is sufficiently dominant past the Balmer limit to ensure that the rest-frame $B-R$ criterion is satisfied.

4.4. An Inflection Resulting from a Nonstellar $T = 10^4$ K Hydrogen Absorption Process

In the previous three sections, we demonstrated that the inflection at H_∞ observed in LRDs can be replicated by models that have sufficiently evolved stellar populations such that they intrinsically have Balmer breaks. However, A-type stars are not the only place where Balmer absorption can occur, and in principle a reservoir of $\sim 10^4$ K gas associated with the accretion disk could produce a feature that looks remarkably similar to a stellar Balmer break by absorbing photons from the AGN continuum. One such model was proposed by K. Inayoshi & R. Maiolino (2025), wherein the accretion disk is embedded in extremely dense gas at this temperature. Such a model can account for the kinematically offset absorption seen in the broad Hα in some systems (e.g., I. Juodžbalis et al. 2024; J. Matthee et al. 2024; B. Wang et al. 2025). An intrinsic inflection in the accretion disk spectrum could also result from an opacity gap from hydrogen at the point where the disk temperature reaches $\sim 10^4$ K (T. A. Thompson et al. 2005). While we do not explore these classes of models in detail, they (and other AGN models that can result in intrinsic breaks at H_∞) merit further exploration given the clear empirical link to a preferred inflection location in LRDs and the wide range in observed changes in spectral shape that occur at this very specific wavelength.

5. Discussion and Conclusions

In this work, we leverage the red selection of RUBIES (A. de Graaff et al. 2025a), supplementing with all public spectra hosted in the DJA, to study the continuum shapes of extremely red sources with strong Hα emission. We find that all unresolved sources that exhibit strong changes in spectral slope in the rest-optical (which we consider to be V-shaped LRDs; e.g., I. Labbe et al. 2025; J. E. Greene et al. 2024; D. D. Kocevski et al. 2025) consistently exhibit that inflection point very near to H_∞, indicating an empirical connection between these changes in slope and $n = 2$ hydrogen. The preference for an inflection point at this very specific wavelength rules out AGN-only models that account for the change with the intersection of a scattered-light component and a highly reddened AGN component, similar to what is seen in more typical extremely red quasars that show no such preference for a specific break location (e.g., R. J. Assef et al. 2016; F. Hamann et al. 2017). This also rules out V-shaped LRDs resulting from the intersection between a young stellar component and an AGN, as these models would suffer from the same lack of a specific preferred inflection location as the aforementioned model.

In contrast, we demonstrate that models where an evolved stellar population dominates the UV through the rest-optical and the reddened AGN component picks up just past the break *can* produce this V shape at H_∞, provided that the AGN is sufficiently reddened. For this scenario to be ubiquitous in the brightest LRDs, there would need to be a link between the age of the stellar population (which must be $\gtrsim$50 Myr) and this particular reddened AGN SED. This model would also have clear observational consequences if the duty cycle of LRDs is $<$100%, because the AGN turning off (and, therefore, LRDs losing the reddened AGN continuum that accounts for the rising SED redward of the break) would leave behind a poststarburst core that remains detectable as a compact, evolved stellar population, unless star formation restarts coincidentally with the AGN shutting down. The massive quiescent galaxy identified in A. Weibel et al. (2024) at $z = 7.3$ *does* strongly match the spectral shape of the L. J. Furtak et al. (2024) LRD (at very similar redshift) up to $\sim$4000 Å, making such a connection plausible. However, it remains to be seen whether the number densities work out for this model to hold for the full population of high-z LRDs.

Additionally, the AGN in composite models is difficult to square with the deficiency of hard X-ray photons from a hot corona (H. B. Akins et al. 2025; T. T. Ananna et al. 2024; L. J. Furtak et al. 2024; R. Maiolino et al. 2025; M. Yue et al. 2024) and the lack of a near-IR (NIR) rise associated with a dusty torus (H. B. Akins et al. 2025; B. Wang et al. 2025; C. C. Williams et al. 2024). Both these problems could potentially be resolved if the AGN torus is cold (e.g., C. M. Casey et al. 2024; Z. Li et al. 2025), possibly due to a super-Eddington accretion disk that is redder than typical quasar spectra (e.g., M. Volonteri et al. 2017; K. Inayoshi et al. 2025; E. Lambrides et al. 2024; P. Madau & F. Haardt 2024; F. Pacucci & R. Narayan 2024). Narrow-line Seyfert 1 galaxies, which are thought to be accreting near the Eddington rate, exhibit characteristically soft X-ray spectra (e.g., D. E. Osterbrock & R. W. Pogge 1985; S. Komossa 2008), and, in general, variability anticorrelates with the Eddington ratio (e.g., H. Benati Gonçalve et al. 2025) in a way that could make such AGN appealing analogs to LRDs. Additionally, X-ray weakness has also been observed in extremely red quasars, though they have more typical hot dust tori that are detected in the MIR (F. Hamann et al. 2017; Y. Ma et al. 2024). However, a precise configuration of stellar age,

galaxy and AGN dust, and relative luminosity is required for such models to achieve the observed breaks without violating some constraint from the rest-optical through the submillimeter.

The class of models that produces these breaks through stellar emission alone also presents a number of unresolved problems. Because they require significant dust (and often dust-obscured star formation) to properly describe the red continuum, they also predict significant submillimeter emission from cold dust (e.g., I. Labbe et al. 2025), and, to date, no LRD has been detected in the FIR, even in stacks (e.g., H. B. Akins et al. 2025; C. C. Williams et al. 2024; I. Labbe et al. 2025), implying very high dust temperatures and low dust masses (C. M. Casey et al. 2024). There is still some room for a red continuum that is dominated by reddened older stellar populations, which could alleviate tension with FIR nondetections, but these models produce a factor of $\sim$100 too few ionizing photons to account for the observed Balmer emission, even if the kinematics and continuum shape are consistent with starlight (Y. Ma et al. 2025).

The stellar masses implied by these galaxy-only models for the brightest LRDs also present a clear problem for galaxy evolution theory, with number densities that imply baryon conversion efficiencies of $\sim$100% (e.g., M. Boylan-Kolchin 2023)—though we note that such early-forming solutions appear at present to describe the star formation histories of some of the most extremely massive quenched galaxies at $z = 3$–5 (A. C. Carnall et al. 2024; K. Glazebrook et al. 2024; A. de Graaff et al. 2025b). Furthermore, LRDs are unresolved in the rest-optical even when subjected to significant lensing (with sizes $<$30 pc; see L. J. Furtak et al. 2024). The combination of these compact sizes with the aforementioned high stellar masses results in extreme stellar densities that essentially require that they be the progenitors of the dense cores of massive elliptical galaxies. Given that the most massive quiescent galaxies observed at $z = 4$–7 *do* have extended stellar mass profiles (with $r_e \sim$ a few hundred parsecs; see A. C. Carnall et al. 2023; A. Weibel et al. 2024; A. de Graaff et al. 2025b), it also implies that if this evolutionary link holds that LRDs must rapidly grow a stellar envelope around their core to match observations, potentially while losing mass in their cores to avoid being overdense (J. F. W. Baggen et al. 2024). Some of this tension with these uncomfortably large masses and densities can potentially be reduced while remaining consistent with local elliptical cores with modifications to the initial mass function (P. van Dokkum & C. Conroy 2024), but it is essential that better constraints be placed on the number densities of both LRDs and early quiescent populations to test whether a progenitor-descendant evolutionary pathway between the two is plausible.

Ultimately, we remain agnostic as to which specific Balmer break process is occurring in LRDs. While we demonstrate that stellar populations which are dominated by A-type stars can describe the rest-frame UV optical spectral shape of LRDs, it also remains possible that some intrinsic AGN-only process involving $\sim 10^4$ K hydrogen absorption could produce the observed shapes. Whatever physical process drives the transition in spectral slope, we stress that the association with this specific inflection point of H_∞ is empirically a necessary component of describing the rest-optical continuum shape of LRDs. Future work leveraging this information along with the full suite of ancillary observations from the X-ray to the FIR/radio will be essential to reconcile the high number densities and unique SEDs of these new and exciting high-z sources.

Acknowledgments

This work is based in part on observations made with the NASA/ESA/CSA James Webb Space Telescope. The data were obtained from the Mikulski Archive for Space Telescopes at the Space Telescope Science Institute, which is operated by the Association of Universities for Research in Astronomy, Inc., under NASA contract NAS 5-03127 for JWST. The specific observations analyzed can be accessed via DOI: 10.17909/0esg-h949. All of the data products presented herein were retrieved from the Dawn JWST Archive (DJA). DJA is an initiative of the Cosmic Dawn Center, which is funded by the Danish National Research Foundation under grant No. 140. We express gratitude toward the members of the GTO, GO, and DDT teams, whose public data we utilized in this work.

Support for this work was provided by The Brinson Foundation through a Brinson Prize Fellowship grant. Support for program No. 4233 was provided by NASA through a grant from the Space Telescope Science Institute, which is operated by the Association of Universities for Research in Astronomy, Inc., under NASA contract NAS 5-03127. This research was supported by the International Space Science Institute (ISSI) in Bern, through ISSI International Team project No. 562. D.S. acknowledges helpful conversations with Xiaohui Fan and Jared Siegel that contributed to the quality of this work, in addition to aesthetic sign-off from Stephanie Permut on the colors of figures. T.B.M. was supported by a CIERA fellowship. The work of CCW is supported by NOIRLab, which is managed by the Association of Universities for Research in Astronomy (AURA) under a cooperative agreement with the National Science Foundation.

Facility: JWST (NIRCam, NIRSpec).

Software: Astropy (Astropy Collaboration et al. 2013, 2018, 2022), `STScI` JWST Calibration Pipeline (https://jwst-pipeline.readthedocs.io/; J. Rigby et al. 2023), `grizli` (github.com/gbrammer/grizli; G. Brammer 2023b) `msaexp` (https://github.com/gbrammer/msaexp; G. Brammer 2023c), Matplotlib (J. D. Hunter 2007), Flexible Stellar Population Synthesis (C. Conroy et al. 2009; C. Conroy & J. E. Gunn 2010), SEDPy (B. D. Johnson 2019).

ORCID iDs

David J. Setton https://orcid.org/0000-0003-4075-7393
Jenny E. Greene https://orcid.org/0000-0002-5612-3427
Anna de Graaff https://orcid.org/0000-0002-2380-9801
Yilun Ma (马逸伦) https://orcid.org/0000-0002-0463-9528
Joel Leja https://orcid.org/0000-0001-6755-1315
Jorryt Matthee https://orcid.org/0000-0003-2871-127X
Rachel Bezanson https://orcid.org/0000-0001-5063-8254
Leindert A. Boogaard https://orcid.org/0000-0002-3952-8588
Nikko J. Cleri https://orcid.org/0000-0001-7151-009X
Harley Katz https://orcid.org/0000-0003-1561-3814
Ivo Labbe https://orcid.org/0000-0002-2057-5376
Michael V. Maseda https://orcid.org/0000-0003-0695-4414
Ian McConachie https://orcid.org/0000-0002-2446-8770

Tim B. Miller https://orcid.org/0000-0001-8367-6265
Sedona H. Price https://orcid.org/0000-0002-0108-4176
Katherine A. Suess https://orcid.org/0000-0002-1714-1905
Pieter van Dokkum https://orcid.org/0000-0002-8282-9888
Bingjie Wang (王冰洁) https://orcid.org/0000-0001-9269-5046
Andrea Weibel https://orcid.org/0000-0001-8928-4465
Katherine E. Whitaker https://orcid.org/0000-0001-7160-3632
Christina C. Williams https://orcid.org/0000-0003-2919-7495

References

Akins, H. B., Casey, C. M., Allen, N., et al. 2023, ApJ, 956, 61
Akins, H. B., Casey, C. M., Lambrides, E., et al. 2025, ApJ, 991, 37
Ananna, T. T., Bogdán, Á., Kovács, O. E., Natarajan, P., & Hickox, R. C. 2024, ApJL, 969, L18
Arrabal Haro, P., Dickinson, M., Finkelstein, S. L., et al. 2023, ApJL, 951, L22
Assef, R. J., Walton, D. J., Brightman, M., et al. 2016, ApJ, 819, 111
Astropy Collaboration, Price-Whelan, A. M., Sipőcz, B. M., et al. 2018, AJ, 156, 123
Astropy Collaboration, Price-Whelan, A. M., Lim, P. L., et al. 2022, ApJ, 935, 167
Astropy Collaboration, Robitaille, T. P., Tollerud, E. J., et al. 2013, A&A, 558, A33
Baggen, J. F. W., van Dokkum, P., Brammer, G., et al. 2024, ApJL, 977, L13
Baggen, J. F. W., van Dokkum, P., Labbé, I., et al. 2023, ApJL, 955, L12
Baldwin, J. A., Ferland, G. J., Martin, P. G., et al. 1991, ApJ, 374, 580
Banerji, M., Alaghband-Zadeh, S., Hewett, P. C., & McMahon, R. G. 2015, MNRAS, 447, 3368
Barro, G., Pérez-González, P. G., Kocevski, D. D., et al. 2024, ApJ, 963, 128
Barrufet, L., Oesch, P., Marques-Chaves, R., et al. 2025, MNRAS, 537, 3453
Benati Gonçalve, H., Panda, S., Storchi Bergmann, T., Cackett, E. M., & Eracleous, M. 2025, ApJ, 988, 27
Bezanson, R., Labbe, I., Whitaker, K. E., et al. 2024, ApJ, 974, 92
Boylan-Kolchin, M. 2023, NatAs, 7, 731
Brammer, G. 2023a, msaexp: NIRSpec Analyis Tools, v0.6.17, Zenodo, doi:10.5281/zenodo.7299500
Brammer, G. 2023b, grizli, v1.8.2, Zenodo, doi:10.5281/zenodo.7712834
Brammer, G. 2023c, msaexp: NIRSpec Analyis Tools, v0.6.17, Zenodo, doi:10.5281/zenodo.7299500
Brooks, M., Simons, R. C., Trump, J. R., et al. 2025, ApJ, 986, 177
Bunker, A. J., Cameron, A. J., Curtis-Lake, E., et al. 2024, A&A, 690, A288
Calzetti, D. 1997, AJ, 113, 162
Carnall, A. C., Cullen, F., McLure, R. J., et al. 2024, MNRAS, 534, 325
Carnall, A. C., McLure, R. J., Dunlop, J. S., et al. 2023, Natur, 619, 716
Casey, C. M., Akins, H. B., Kokorev, V., et al. 2024, ApJL, 975, L4
Chabrier, G. 2003, PASP, 115, 763
Conroy, C., & Gunn, J. E. 2010, ApJ, 712, 833
Conroy, C., Gunn, J. E., & White, M. 2009, ApJ, 699, 486
de Graaff, A., Brammer, G., Weibel, A., et al. 2025a, A&A, 697, A189
de Graaff, A., Setton, D. J., Brammer, G., et al. 2025b, NatAs, 9, 280
Eisenstein, D. J., Willott, C., Alberts, S., et al. 2023, arXiv:2306.02465
Foreman-Mackey, D., Hogg, D. W., Lang, D., & Goodman, J. 2013, PASP, 125, 306
Furtak, L. J., Labbé, I., Zitrin, A., et al. 2024, Natur, 628, 57
Furtak, L. J., Zitrin, A., Plat, A., et al. 2023, ApJ, 952, 142
Gentile, F., Casey, C. M., Akins, H. B., et al. 2024, ApJL, 973, L2
Glazebrook, K., Nanayakkara, T., Schreiber, C., et al. 2024, Natur, 628, 277
Glikman, E., Urrutia, T., Lacy, M., et al. 2012, ApJ, 757, 51
Greene, J. E., Labbe, I., Goulding, A. D., et al. 2024, ApJ, 964, 39
Hamann, F., Zakamska, N. L., Ross, N., et al. 2017, MNRAS, 464, 3431
Harikane, Y., Zhang, Y., Nakajima, K., et al. 2023, ApJ, 959, 39
Hinshaw, G., Larson, D., Komatsu, E., et al. 2013, ApJS, 208, 19
Hunter, J. D. 2007, CSE, 9, 90
Hviding, R. E., de Graaff, A., Miller, T. B., et al. 2025, A&A, 702, A57
Inayoshi, K., Kimura, S. S., & Noda, H. 2025, PASJ, 77, 811
Inayoshi, K., & Maiolino, R. 2025, ApJL, 980, L27
Johnson, B. D., 2019 SEDPY: Modules for Storing and Operating on Astronomical Source Spectral Energy Distribution, Astrophysics Source Code Library, ascl:1905.026
Juodžbalis, I., Ji, X., Maiolino, R., et al. 2024, MNRAS, 535, 853
Katz, H., Cameron, A. J., Saxena, A., et al. 2025, OJAp, 8, 104
Killi, M., Watson, D., Brammer, G., et al. 2024, A&A, 691, A52
Kocevski, D. D., Finkelstein, S. L., Barro, G., et al. 2025, ApJ, 986, 126
Kokorev, V., Caputi, K. I., Greene, J. E., et al. 2024, ApJ, 968, 38
Kokorev, V., Fujimoto, S., Labbe, I., et al. 2023, ApJL, 957, L7
Kokubo, M., & Harikane, Y. 2024, arXiv:2407.04777
Komossa, S. 2008, RMxAA, 32, 86
Kriek, M., & Conroy, C. 2013, ApJL, 775, L16
Kubota, A., & Done, C. 2018, MNRAS, 480, 1247
Labbe, I., Greene, J. E., Bezanson, R., et al. 2025, ApJ, 978, 92, submitted
Labbé, I., van Dokkum, P., Nelson, E., et al. 2023, Natur, 616, 266
Lambrides, E., Garofali, K., Larson, R., et al. 2024, arXiv:2409.13047
Larson, R. L., Finkelstein, S. L., Kocevski, D. D., et al. 2023, ApJL, 953, L29
Li, Z., Inayoshi, K., Chen, K., Ichikawa, K., & Ho, L. C. 2025, ApJ, 980, 36
Lin, X., Wang, F., Fan, X., et al. 2024, ApJ, 974, 147
Ma, Y., Goulding, A., Greene, J. E., et al. 2024, ApJ, 974, 225
Ma, Y., Greene, J. E., Setton, D. J., et al. 2025, ApJ, 981, 191
Madau, P., & Haardt, F. 2024, ApJL, 976, L24
Maiolino, R., Risaliti, G., Signorini, M., et al. 2025, MNRAS, 538, 1921
Maseda, M. V., de Graaff, A., Franx, M., et al. 2024, A&A, 689, A73
Matthee, J., Naidu, R. P., Brammer, G., et al. 2024, ApJ, 963, 129
Meena, A. K., Zitrin, A., Jiménez-Teja, Y., et al. 2023, ApJL, 944, L6
Nanayakkara, T., Glazebrook, K., Jacobs, C., et al. 2024, NatSR, 14, 3724
Noll, S., Burgarella, D., Giovannoli, E., et al. 2009, A&A, 507, 1793
Onoue, M., Inayoshi, K., Ding, X., et al. 2023, ApJL, 942, L17
Osterbrock, D. E., & Pogge, R. W. 1985, ApJ, 297, 166
Pacucci, F., & Narayan, R. 2024, ApJ, 976, 96
Pérez-González, P. G., Barro, G., Rieke, G. H., et al. 2024, ApJ, 968, 4
Price, S. H., Bezanson, R., Labbe, I., et al. 2025, ApJ, 982, 51
Rigby, J., Perrin, M., McElwain, M., et al. 2023, PASP, 135, 048001
Temple, M. J., Hewett, P. C., & Banerji, M. 2021, MNRAS, 508, 737
Thompson, T. A., Quataert, E., & Murray, N. 2005, ApJ, 630, 167
Übler, H., Maiolino, R., Pérez-González, P. G., et al. 2024, MNRAS, 531, 355
Valentino, F., Brammer, G., Gould, K. M. L., et al. 2023, ApJ, 947, 20
van Dokkum, P., & Conroy, C. 2024, ApJL, 973, L32
Veilleux, S., Trippe, M., Hamann, F., et al. 2013, ApJ, 764, 15
Volonteri, M., Reines, A. E., Atek, H., Stark, D. P., & Trebitsch, M. 2017, ApJ, 849, 155
Volonteri, M., Trebitsch, M., Dubois, Y., et al. 2025, A&A, 695, A33
Wang, B., de Graaff, A., Davies, R. L., et al. 2025, ApJ, 984, 121
Wang, B., Leja, J., de Graaff, A., et al. 2024b, ApJL, 969, L13
Weaver, J. R., Cutler, S. E., Pan, R., et al. 2024, ApJS, 270, 7
Weibel, A., de Graaff, A., Setton, D. J., et al. 2024, arXiv:2409.03829
Williams, C. C., Alberts, S., Ji, Z., et al. 2024, ApJ, 968, 34
Yue, M., Eilers, A.-C., Ananna, T. T., et al. 2024, arXiv:2404.13290